Title

Development and testing of hyperpolarized 13C MR calibrationless parallel imaging

Authors

Feng, Yesu

Gordon, Jeremy W

Shin, Peter J

et al.

Publication Date

2016

DOI

10.1016/j.jmr.2015.10.018

Peer reviewed

HHS Public Access

Author manuscript

J Magn Reson. Author manuscript; available in PMC 2017 January 01.

Published in final edited form as:

J Magn Reson. 2016 January ; 262: 1–7. doi:10.1016/j.jmr.2015.10.018.

Development and testing of hyperpolarized ^{13}C MR calibrationless parallel imaging

Yesu Feng[a], **Jeremy W. Gordon**[a], **Peter J. Shin**[a], **Cornelius von Morze**[a], **Michael Lustig**[b], **Peder E.Z. Larson**[a], **Michael A. Ohliger**[a], **Lucas Carvajal**[a], **James Tropp**[c], **John M. Pauly**[d], and **Daniel B. Vigneron**[a,*]

[a]Department of Radiology and Biomedical Imaging, UCSF, San Francisco, CA, USA

[b]Department of Electrical Engineering and Computer Sciences, UC Berkeley, Berkeley, CA, USA

[c]GE Healthcare, Fremont, CA, USA

[d]Department of Electrical Engineering, Stanford University, Stanford, CA, USA

Abstract

A calibrationless parallel imaging technique developed previously for ^{1}H MRI was modified and tested for hyperpolarized ^{13}C MRI for applications requiring large FOV and high spatial resolution. The technique was demonstrated with both retrospective and prospective under-sampled data acquired in phantom and *in vivo* rat studies. A 2-fold acceleration was achieved using a 2D symmetric EPI readout equipped with random blips on the phase encode dimension. Reconstructed images showed excellent qualitative agreement with fully sampled data. Further acceleration can be achieved using acquisition schemes that incorporate multi-dimensional under-sampling.

Keywords

Hyperpolarization; Carbon-13; Parallel imaging

1. Introduction

Hyperpolarized (HP) ^{13}C techniques [1] increase spin magnetization for ^{13}C nuclei by several orders of magnitude compared to polarization achieved at thermal equilibrium. This dramatic signal enhancement has enabled *in vivo* magnetic resonance imaging (MRI) and spectroscopy (MRS) of ^{13}C labeled biomolecules with high contrast and temporal resolution [2–5]. Nevertheless, the short time window due to T_1 relaxation and metabolism presents a significant challenge to these techniques [3,4,6–12]. Fast data acquisition is imperative to mitigate signal loss due to relaxation and to measure rapid *in vivo* substrate uptake and metabolic conversion rates. Current methods have worked adequately in preclinical animal studies with fields-of-view (FOVs) less than 10 cm and coarse resolution, but much larger FOV's with high spatial resolution is needed for future clinical studies.

*Corresponding author at: Byers Hall Suite 102, 1700 4th St., San Francisco, CA 94158, USA. dan.vigneron@ucsf.edu. .

Parallel imaging schemes with multi-channel coils offer the potential for improved spatial coverage and high acceleration while maintaining high SNR. However, the transient nature of HP ^{13}C signal presents a new obstacle to parallel imaging. Traditional SENSE [13] or SMASH [14]-based reconstruction techniques use *a priori* knowledge of coil sensitivity, which is typically acquired in a calibration scan obtained prior to the actual scan. However, there is insufficient endogenous ^{13}C signal for coil sensitivity calibration prior to injection of HP substrate, at which time a separate calibration scan is impractical due to the limited HP magnetization time and the desire to acquire dynamic metabolic data throughout the time following injection. Alternatively, an external ^{13}C phantom can be used [15], but this approach is complicated by the low sensitivity of ^{13}C nuclei and variations in coil shape and/or position between the calibration and actual scans, which are especially problematic with the use of flexible coils that are highly desirable for clinical studies. Auto-calibrated reconstruction techniques such as GRAPPA and SPIRiT [16–19] incorporate fully-sampled auto-calibration scan (ACS) regions into the acquired data and effectively overcome the need for a separate reference. Yet, the amount of required ACS data is substantial given the low matrix sizes in ^{13}C studies, greatly limiting the efficiency and effective SNR for HP ^{13}C imaging.

Recently, a new class of parallel imaging techniques has been reported that does not require explicit calibration of coil sensitivity. Shin et al. [20] proposed the Simultaneous Auto-calibrating and K-space Estimation (SAKE) method, which provides implicit calibration by recasting k-space data into a structured low-rank matrix. Trzasko et al. [21] described another method named Calibration-free Locally low-rank Encouraging Reconstruction (CLEAR), which explores the local low-rankness of k-space data. Both methods overcome the need for a separate calibration step.

The goal of this study was to validate the efficacy of the SAKE calibrationless parallel imaging acceleration strategy for hyperpolarized ^{13}C imaging, as acquiring large clinical sized FOVs with fine spatial resolution will be critical for clinical translation to patient studies. For this proof-of-concept study, we designed an acquisition scheme with a single-shot 2D symmetric EPI readout to achieve a 2-fold acceleration on the phase encode dimension and tested this approach with its requisite reconstruction method in both phantoms and *in vivo* animal studies. We demonstrate that the scheme can be applied both for hyperpolarized metabolic agents (pyruvate) as well as perfusion agents such as t-butanol, which is more diffusible especially in brain tissue compared with pyruvate and urea [22,23].

2. Materials and methods

2.1. Hardware setup

All scans were acquired using a 3T scanner (MR750, GE Healthcare) equipped with multi-nuclear capability. Proton MR anatomical images were acquired with the built-in body coil. For ^{13}C RF excitation, a custom-designed ^{13}C transmitter was used [15]. This transmitter coil consists of a Helmholtz resonant pair in which two loops are arranged in a clamshell manner mounted on a dedicated patient cradle for volumetric transmission. The transmitter coil was dynamically detuned at the time of reception. For ^{13}C receive, an 8-channel array coil was used with 2 sets of four coil elements in a linear arrangement as shown in Fig. 1(a)

[24,25]. Each rectangular element was approximately 5 × 10 cm and adjacent elements were overlapped to minimize mutual inductance. The total length of each panel was around 18 cm [24].

2.2. Hyperpolarization

For the phantom study, 1.47 g [1-^{13}C] pyruvate mixed with 15 mM OX063 radical (GE Healthcare) was hyperpolarized in a 5 T SpinLab DNP polarizer (GE Healthcare) for 2 h and then dissolved into a 40 ml aqueous solution of 250 mM hyperpolarized [1-^{13}C] pyruvate. The solution was immediately injected (within 5 s) into a plastic sphere (~10 cm diameter) containing 400 ml water (Fig. 1(c)). The final phantom solution contained about 440 ml of 23 mM hyperpolarized [1-^{13}C]pyruvate.

For the *in vivo* study, 110 mg of mixed ^{13}C-t-butanol, glycerol (t-butanol and glycerol are 1:1 by volume) and 15 mM 'Finland' trityl radical (Oxford Instruments) were polarized in a HyperSense DNP polarizer (Oxford instruments) for 1.5 h and then dissolved with 5 ml phosphate-buffered saline. The final solution containing 100 mM ^{13}C-t-butanol was then carried to the scanner and ~3.0 ml of this solution was injected into the rat through a tailvein catheter over a period of 12 s. The polarization level for both [1-^{13}C]pyruvate and ^{13}C-t-butanol was approximately 20%.

2.3. Symmetric, ramp-sampled EPI

In this study, we applied a symmetric, ramp-sampled EPI sequence [26] to acquire fast MR molecular imaging of HP ^{13}C substrates. To correct for the timing inconsistencies between odd and even echoes, a reference scan without phase encoding from the hyperpolarized substrate was acquired immediately after the image acquisition.

2.4. Thermally polarized phantom study

The phantom used consisted of two bottles and four small tubes filled with thermally polarized ethylene glycol as shown in Fig. 1 (b). Due to the low sensitivity of natural abundance ^{13}C in ethylene glycol, a 12 cm axial slab was excited using a 45° spectral-spatial pulse and signal was averaged over 13 min. The spectral-spatial pulse was designed for hyperpolarized imaging of [1-^{13}C]pyruvate and metabolites at 3T, with a passband full-width at half-maximum of 120 Hz and a stopband of 600 Hz. This passband was sufficiently narrow to excite only the central ^{13}C resonance of ethylene glycol. The typical linewidth of ^{13}C spectra at the 3T scanner is around 10 Hz (~0.3 ppm). A FOV of 16 × 16 cm^2 was acquired using the aforementioned ^{13}C-EPI sequence with a 64 × 64 (fully sampled) matrix. The effective TE was 40 ms with an echo spacing of 1.3 ms, with a readout bandwidth of 166 kHz. A reference scan for the EPI reconstruction was acquired at the end of the scan with the same excitation pulse.

2.5. Hyperpolarized ^{13}C-pyruvate phantom study

Acquisition started 30 s after the injection of HP ^{13}C-pyruvate to minimize turbulence and ensure sufficient mixing with the solvent. A 15 mm axial slice across the spherical phantom containing 440 mL aqueous solution of 23 mM HP [1-^{13}C]pyruvate was excited using a 45° spectral-spatial pulse. A FOV of 16 × 16 cm^2 was acquired with a 64 × 32 (2-fold under-

sampling in the phase encode direction as described in the image reconstruction session below) matrix using the same EPI readout as that used in the thermal phantom study, with an effective TE of 20 ms. And the data was subsequently reconstructed to a 64 × 64 matrix (2.5 × 2.5 mm^2 resolution). The reference scan was acquired immediately after the under-sampled scan with the same excitation pulse.

2.6. In vivo hyperpolarized ^{13}C-t-butanol study

All animal studies were carried out under protocols approved by the UCSF Institutional Animal Care and Use Committee. A normal Sprague–Dawley rat was placed on a heating pad atop one of the paddle receiver and anesthetized with 1.5% of isoflurane delivered via nose cone (flow rate 1 L/min). The rat was positioned supine with its head and tail positioned to the right and left respectively looking into the magnet bore (Fig. 1(d)). The proton anatomical images were acquired using a T_2-weighted 2D Fast Spin Echo (FSE) sequence. For the HP ^{13}C experiment, a coronal slice with 2 cm thickness was excited with a 20 × 20 cm^2 FOV and 3.1 × 3.1 mm^2 in-plane resolution (Fig. 6(b)). Imaging was initiated 20 s after the start of injection with a 12.8 ms 60° sinc pulse to excite a 15 mm coronal slice, followed by a symmetric, ramp-sampled EPI readout that covered a FOV of 20 × 20 cm^2 with a 64 × 32 matrix size (2-fold undersampling in the phase encode direction) with an effective TE of 26 ms, an echo spacing of 1.1 ms and a readout bandwidth of 200 kHz. The total TR was 200 ms. As in the phantom study, a reference scan was acquired for the symmetric EPI. Lastly, a separate scan using partial Fourier acquisition (TE = 26 ms) with 25% over-sampling in the phase-encode direction was acquired to compare with SAKE reconstruction.

2.7. Image reconstruction

Ramp-sampled EPI data were interpolated to a Cartesian k-space grid and corrected for timing delays using the Orchestra reconstruction toolbox (GE Healthcare, WI, USA). Partial Fourier k-space data was reconstructed with homodyne processing using the Orchestra toolbox while the under-sampled k-space data were first zero-filled to a 64 × 64 matrix and subsequently reconstructed with SAKE or GRAPPA algorithm using MATLAB before 2D Fourier transform.

For the thermal phantom study, different undersampling patterns were applied *retrospectively* to the acquired data. The 2-fold undersampling pattern for SAKE (Fig. 3(d)) was derived from a central line across a 2D variable density Poisson-disc undersampling pattern [27], which is known to provide a high degree of incoherence and has been generally applied to compressed sensing[28,29]. We also generated a 3-fold undersampling pattern for SAKE (Fig. 3(e)) by skipping more lines in the peripheral region of the 2-fold pattern. For GRAPPA reconstruction, we generated 2 undersampling patterns with fully sampled ACS areas. The first one had 16 calibration lines and the outer k-space was 3-fold under sampled for a 2-fold overall acceleration (Fig. 3(b)) and the second had 12 calibration lines and the outer k-space was 4-fold under sampled for a 2.6-fold overall acceleration (Fig. 3(c)). Reconstruction coefficients were estimated with these ACS lines using a 4-by-3 kernel (4 phase encoding and 3 frequency encoding neighbor data points). For the hyperpolarized

studies, only the 2-fold SAKE variable-density pattern (Fig. 3(d)) was used for *prospective* data undersampling.

A prior publication [20] detailed a formal treatment of SAKE reconstruction theory and its application to ^{1}H MRI. The reconstruction algorithm reduces ultimately to the following optimization problem:

$$\begin{aligned} &min\|Dx-y\|^2 \\ &\text{s.t.} rank\,(A)=k, \\ &x=H^+(A) \end{aligned} \quad (1)$$

where the least squares objective function enforces data consistency between the reconstructed k-space data x and acquired data y, which are related by the sampling operator D. A is the structured low-rank matrix generated by sliding a multi-channel window across the k-space data x. Such operation, represented by operator H gives rise to stacked, block-wise Hankel structure in A and H^+ denotes the inverse projection from A to x. The Block Hankel matrix is known [30] to possess well defined subspaces and the first equality constraint ensures its low rank property. As coil sensitivities vary smoothly in the image domain, we can assume that the bandwidths in k-space of all the coils are bound by some small number s. Then, it was shown in the previous study [20] that we can choose a large enough window size w to make the block Hankel matrix A to be a low rank matrix with its rank k bound by $(w+s-1)^2$. Therefore, the window-size normalized rank is bound by $(w+s-1)^2/w^2$. Accordingly, as the window size w increases, the normalized rank shrinks towards one, leading to a more compact signal subspace. In addition, the rank value is affected by the object size with smaller object size giving rise to lower rank value. In the current study, based on the object size and coil set-up, a 6 × 6 (w^2) window was used to slide across the acquired k-space data. This window size (6 × 6) was chosen to guarantee a compact signal space while keeping the reconstruction time short, as larger window size (e.g., 8 × 8) significantly increases computation time. The k-space data matrix has a size of $N_x \times N_y N_c$ (64 × 64 × 8) where N_x and N_y are the readout and phase encode dimensions and N_c is the number of elements. The generated A matrix has size $w^2N_c \times (N_x - w + 1)(N_y + w + 1)$, resulting in 288 × 3481 for the current study.

This optimization was implemented using the Cadzow [31] algorithm, which is an alternating projection method. The iteration begins with projecting the zero-filled multi-channel k-space data matrix x onto data matrix A. Then with assumed rank value as discussed below, a hard thresholding on singular values was applied to A to enforce the low rankness projection. Lastly, an inverse transform converts the Hankel matrix back to k-space and consistency between reconstructed (x) and acquired data (y) was imposed. The reconstruction terminates either when the change between two consecutive iterations falls below a certain threshold or upon the request from user after a certain number of iterations. *As a priori* knowledge of the rank value is required for the retrospectively under-sampled data (Section 3.1), it was estimated (1.1 normalized against window size, w^2) based on SVD of fully sampled data. As shown in Fig. 4, it was chosen at the turning point of the SVD plot such that all dominant singular values are considered as in the signal space. Without fully

sampled data, the rank for the prospectively under-sampled data (Sections 3.2 and 3.3) cannot be estimated the same way. However, we assume the same value is valid due to the very comparable size of all studied objects within the chosen FOV. An effective method to de-noise image without sacrificing small signal is to impose sparsity in some transformed domain (e.g., wave-lets). Due to the relatively low SNR in the *in vivo* study, a joint-sparsity model (Ref. [27]) was adopted and a generalized l_1-norm regularization was incorporated into the general SAKE reconstruction. The regularized optimization problem is:

$$\begin{aligned} &min\|D(x)-y\|^2+\lambda\sum_r\sqrt{\sum_c\Psi|\{IFFT(x)\}|^2} \\ &\text{s.t.}\,rank(A)=k \\ &x=H^+(A) \end{aligned} \tag{2}$$

Here Ψ denotes the transform from image domain to wavelets domain and r and c are indices for the spatial and coil element dimensions, respectively. λ controls the compromise between the *a priori* knowledge of sparsity and the data consistency constraint.

3. Results

3.1. SAKE reconstruction on retrospectively under-sampled phantom data

Fully sampled images from individual coils are shown in Fig. 2. Comparison between the square root of the sum of squares (ssos) image from the fully sampled data and the images from SAKE and GRAPPA reconstruction are shown in Fig. 3. The undersampling patterns are inserted into panels (b)–(e) of Fig. 3. Notably, as opposed to GRAPPA (Fig. 3(b) and (c)), no fully sampled ACS was required for SAKE (Fig. 3(d) and (e)). Accordingly, with the same overall acceleration rate, undersampling patterns for SAKE are more flexible and can better cover the peripheral region of k-space. As shown in Fig. 3, performance of SAKE and GRAPPA against 2-fold under-sampled data are comparable (Fig. 3(b) and (d)) with mean square errors (MSE) of 2.70×10^{-4} and 2.67×10^{-4}, respectively, compared to the ssos image. However, with an ACS of 12 lines, GRAPPA failed (Fig. 3(c), MSE = 2.70×10^{-3}) at an overall acceleration rate of 2.6 due to aggressive under-sampling of the outer k-space (4-fold). Even with 3-fold acceleration, SAKE still largely suppressed aliasing artifact across the phase encode direction (Fig. 3(e), MSE = 4.38×10^{-4}).

For SAKE reconstruction, a 6 × 6 window size was chosen empirically to generate a low-rank block Hankel data matrix A (Eq. (2)). The window-size normalized rank was chosen to be 1.1. As shown in Fig. 4(a), this rank value was chosen at the “elbow point” in the singular value distribution curve of the *fully* sampled data matrix to separate the signal space and the noise space. This rank value however, cannot be directly estimated from the under-sampled data in general, since undersampling has obscured the transition between dominant and non-dominant singular values [20,32] (Fig. 4(b)). The iterative reconstruction of SAKE converged within 25 s on a MacBook Pro equipped with 2.2 GHz quad-core Intel Core i7 processor.

3.2. SAKE reconstruction on prospectively under-sampled phantom data

Due to variations between dissolutions, specifically sample transfer time and polarization levels between hyperpolarized studies, no fully sampled image was acquired to benchmark reconstruction on the prospectively under-sampled data. The zero-filled and SAKE reconstructed images of HP ^{13}C-pyruvate phantom (Fig. 1(c)) are shown in Fig. 5. The sampling pattern is the same as that shown in Fig. 3(d). The image was acquired with a single scan using the same FOV and matrix size as the ethylene glycol study. SAKE reconstruction assumed the same parameters, but converged slowly (~150 s), which is not unexpected due to the slightly larger object size compared to the thermal ethylene glycol phantom. The SAKE reconstruction shows no aliasing artifacts in the phase encode direction that would indicate a failure in the reconstruction, and the sharp edge of the phantom is clearly delineated. The dark line near the top left corner is likely due to B_0 inhomogeneity or turbulence in the phantom that resulted in imperfect excitation given by the aforementioned spectral-spatial pulse.

3.3. SAKE reconstruction of in vivo HP ^{13}C-t-butanol data

^{13}C-t-butanol is considered freely diffusible and has been previously used for hyperpolarized *in vivo* perfusion studies[22,23]. As opposed to most other hyperpolarized ^{13}C molecules, such as ^{13}C-urea, ^{13}C-t-butanol quickly crosses the blood brain barrier and therefore generates strong signal in brain as well as in other organs (e.g., kidney). Moreover, since t-butanol is not metabolized *in vivo*, it suffers no signal loss due to metabolism as metabolic agents do (e.g., pyruvate to lactate). As shown in Fig. 6 (e) and (f), high signal intensity was observed in the rat kidneys and brain. The co-registration of ^{13}C signal is reasonable considering the different slice thickness for the proton FSE (2 mm) and ^{13}C EPI images (15 mm). The two kidneys were not symmetrical in the image due to the non-planar orientation of the rat and the thin slice for proton image. Evident aliasing due to under sampling can be seen in the zero-filled image (Fig. 6(a)) but is suppressed in SAKE reconstructed image (Fig. 6(b)). Notably, the SAKE reconstruction, which converges within 30 s, shows better differentiation between the renal cortex and inner medulla compared to the data acquired with partial Fourier coverage (compare the kidney in the lower right position in Fig. 6(e) and (f)). The effective echo time (TE) of the SAKE scan is comparable to that of the partial Fourier acquisition (75% partial Fourier fraction). However, a quantitative comparison is difficult due to the enhanced SNR of SAKE reconstruction due to SVD thresholding as well as the enforced sparsity by wavelet transform. Here the regularization parameter λ in Eq. (2) was empirically chosen to be 0.32. The signal intensity ratio of kidney versus brain is comparable in SAKE (0.93) and the partial Fourier acquisition (1.08), which was calculated using the two ROIs in Fig. 6(e) and (f).

4. Discussion

A major challenge facing clinical studies using hyperpolarized ^{13}C MR molecular imaging is the need to acquire the prepolarized, high SNR signals with adequate spatial coverage while maintaining high temporal and spatial resolution. Fast acquisition techniques such as EPI and parallel imaging with multichannel coils have the potential to address these challenges. A previous ^{1}H MRI study [20] demonstrated the SAKE reconstruction for 2D

accelerated, proton image acquisition with both Cartesian and non-Cartesian k-space coverage (e.g., spiral). The goal of this study was to apply this calibration-less parallel imaging approach to HP ^{13}C studies. HP ^{13}C studies have a critical demand of acquisition speed given the short T_1 lifetime and low gyromagnetic ratio of ^{13}C spins; the former limits the time window for signal acquisition and the latter puts a constraint on the achievable speed to traverse k-space due to limited gradient strength on clinical scanners. Therefore, a sub-Nyquist sampling strategy is beneficial, especially when a large FOV with fine spatial resolution is desirable such as in clinical human studies. As an initial, proof-of-concept demonstration, we applied SAKE reconstruction to a 2D symmetric EPI readout with a 2-fold under sampling on the phase encode direction. As shown above, this reconstruction strategy does not require explicit calibration and is robust against aliasing due to under sampling. This gives SAKE a unique advantage over conventional parallel imaging schemes that require separate calibration scans. As shown in this study, to keep up with the same acceleration factor, GRAPPA with a typical ACS of 10–20 lines needs to aggressively under-sample the peripheral region of k-space, leading to loss of fine structure and unrecovered aliasing artifacts.

This calibration-less parallel imaging approach can also be applied to HP ^{13}C MRI data acquired with multi-dimensional acceleration, especially as higher channel count coils are developed. While higher 1D acceleration rates (e.g., 2.5 or 3-fold, as demonstrated in this study) for SAKE are achievable with the current coil setup, sequences such as a 3D multi-shot EPI offer the potential of even greater acceleration since incoherent undersampling can be performed on both phase-encode dimensions. With multi-shot excitation, one can also expect improved SNR when this undersampling strategy is combined with a tailored variable flip angle (VFA) schedule to efficiently allocate full HP magnetization to fewer excitations.

5. Conclusion

In this study, we investigated a calibrationless parallel imaging method (SAKE) for hyperpolarized ^{13}C imaging. We implemented and tested this technique using a symmetric EPI readout with 2-fold random undersampling in the phase encoding direction. Future work will focus on applying this technique to 3D acquisitions with 2D under-sampling, which is expected to result in further acceleration and improved SNR.

Acknowledgment

This work was supported by NIH Grants R01EB017449, P41EB013598, R01CA183071 and R01EB016741.

References

[1]. Ardenkjær Larsen JH, Fridlund B, Gram A, Hansson G, Hansson L, Lerche MH, et al. Increase in signal-to-noise ratio of >10,000 times in liquid-state NMR. Proc. Natl. Acad. Sci. 2003; 100:10158–10163. [PubMed: 12930897]

[2]. Golman K, in‘t Zandt R, Lerche M, Pehrson R, Ardenkjaer-Larsen JH. Metabolic imaging by hyperpolarized C-13 magnetic resonance imaging for in vivo tumor diagnosis. Cancer Res. 2006; 66:10855–10860. http://dx.doi.org/10.1158/0008-5472.CAN-06-2564. [PubMed: 17108122]

[3]. Kurhanewicz J, Vigneron DB, Brindle K, Chekmenev EY, Comment A, Cunningham CH, et al. Analysis of cancer metabolism by imaging hyperpolarized nuclei: prospects for translation to

clinical research. Neoplasia. 2011; 13:81–97. http://dx.doi.org/10.1593/neo.101102. [PubMed: 21403835]

[4]. Keshari KR, Wilson DM. Chemistry and biochemistry of 13C hyperpolarized magnetic resonance using dynamic nuclear polarization. Chem. Soc. Rev. 2014; 43:1627–1659. http://dx.doi.org/10.1039/c3cs60124b. [PubMed: 24363044]

[5]. Brindle KM, Bohndiek SE, Gallagher FA, Kettunen MI. Tumor imaging using hyperpolarized 13C magnetic resonance spectroscopy. Magn. Reson. Med.: Off. J. Soc. Magn. Reson. Med./Soc. Magn. Reson. Med. 2011; 66:505–519. http://dx.doi.org/10.1002/mrm.22999.

[6]. Feng Y, Davis RM, Warren WS. Accessing long-lived nuclear singlet states between chemically equivalent spins without breaking symmetry. Nat. Phys. 2012; 8:831–837. http://dx.doi.org/10.1038/nphys2425. [PubMed: 23505397]

[7]. Feng Y, Theis T, Liang X, Wang Q, Zhou P, Warren WS. Storage of hydrogen spin polarization in long-lived 13C 2singlet order and implications for hyperpolarized magnetic resonance imaging. J. Am. Chem. Soc. 2013; 135:9632–9635. http://dx.doi.org/10.1021/ja404936p. [PubMed: 23781874]

[8]. Feng Y, Theis T, Wu T-L, Claytor K, Warren WS. Long-lived polarization protected by symmetry. J. Chem. Phys. 2014; 141:134307. http://dx.doi.org/10.1063/1.4896895. [PubMed: 25296806]

[9]. Claytor K, Theis T, Feng Y, Warren W. Measuring long-lived 13C2 state lifetimes at natural abundance. J. Magn. Reson. 2014; 239:81–86. http://dx.doi.org/10.1016/j.jmr.2013.12.009. [PubMed: 24457544]

[10]. Theis T, Feng Y, Wu T, Warren WS. Composite and shaped pulses for efficient and robust pumping of disconnected eigenstates in magnetic resonance. J. Chem. Phys. 2014; 140:014201. http://dx.doi.org/10.1063/1.4851337. [PubMed: 24410222]

[11]. Claytor K, Theis T, Feng Y, Yu J, Gooden D, Warren WS. Accessing long-lived disconnected spin-1/2 eigenstates through spins > 1/2. J. Am. Chem. Soc. 2014; 136:15118–15121. http://dx.doi.org/10.1021/ja505792j. [PubMed: 25229309]

[12]. Zhou X, Graziani D, Pines A. Hyperpolarized xenon NMR and MRI signal amplification by gas extraction. Proc. Natl. Acad. Sci. 2009; 106:16903–16906. http://dx.doi.org/10.1073/pnas.0909147106. [PubMed: 19805177]

[13]. Pruessmann KP, Weiger M, Scheidegger MB, Boesiger P. SENSE: sensitivity encoding for fast MRI. Magn. Reson. Med.: Off. J. Soc. Magn. Reson. Med./Soc. Magn. Reson. Med. 1999; 42:952–962. http://dx.doi.org/10.1002/(sici)1522-2594(199911)42:5<952::aid-mrm16>3.0.co;2-s.

[14]. Sodickson DK, Manning WJ. Simultaneous acquisition of spatial harmonics (SMASH): fast imaging with radiofrequency coil arrays. Magnetic Reson. Med.: Off. J. Soc. Magn. Reson. Med./Soc. Magn. Reson. Med. 1997; 38:591–603. http://dx.doi.org/10.1002/mrm.1910380414.

[15]. Tropp J, Lupo JM, Chen A, Calderon P, McCune D, Grafendorfer T, et al. Multi-channel metabolic imaging, with SENSE reconstruction, of hyperpolarized [1-^{13}C] pyruvate in a live rat at 3.0tesla on a clinical MR scanner. J. Magn. Reson. 2011; 208:171–177. http://dx.doi.org/10.1016/j.jmr.2010.10.007. [PubMed: 21130012]

[16]. Lustig M, Pauly JM. SPIRiT: iterative self-consistent parallel imaging reconstruction from arbitrary k-space. Magn. Reson. Med.: Off. J. Soc. Magn. Reson. Med./Soc. Magn. Reson. Med. 2010; 64:457–471. http://dx.doi.org/10.1002/mrm.22428.

[17]. Jakob PM, Griswold MA, Edelman RR, Sodickson DK. AUTO-SMASH: a self-calibrating technique for SMASH imaging. Magn. Reson. Mater. Phys. Biol. Med. 1998; 7:42–54.

[18]. Heidemann RM, Griswold MA, Haase A, Jakob PM. VD-AUTO-SMASH imaging. Magn. Reson. Med.: Off. J. Soc. Magn. Reson. Med./Soc. Magn. Reson. Med. 2001; 45:1066–1074. http://dx.doi.org/10.1002/mrm.1141.

[19]. Griswold MA, Jakob PM, Heidemann RM, Nittka M, Jellus V, Wang J, et al. Generalized autocalibrating partially parallel acquisitions (GRAPPA). Magn. Reson. Med.: Off. J. Soc. Magn. Reson. Med./Soc. Magn. Reson. Med. 2002; 47:1202–1210. http://dx.doi.org/10.1002/mrm.10171.

[20]. Shin PJ, Larson PEZ, Ohliger MA, Elad M, Pauly JM, Vigneron DB, et al. Calibrationless parallel imaging reconstruction based on structured low-rank matrix completion. Magn. Reson.

Med.: Off. J. Soc. Magn. Reson. Med./Soc. Magn. Reson. Med. 2014; 72:959–970. http://dx.doi.org/10.1002/mrm.24997.

[21]. Trzasko, JD.; Manduca, A. Calibrationless parallel MRI using CLEAR. 2011 45th Asilomar Conference on Signals, Systems and Computers; 2011; p. 75-79.doi:http://dx.doi.org/10.1109/ACSSC.2011.6189958

[22]. Grant AK, Vinogradov E, Wang X, Lenkinski RE, Alsop DC. Perfusion imaging with a freely diffusible hyperpolarized contrast agent. Magn. Reson. Med.: Off. J. Soc. Magn. Reson. Med./Soc. Magn. Reson. Med. 2011; 66:746–755. http://dx.doi.org/10.1002/mrm.22860.

[23]. von Morze C, Bok RA, Reed GD, Ardenkjaer-Larsen JH, Kurhanewicz J, Vigneron DB. Simultaneous multiagent hyperpolarized C-13 perfusion imaging. Magn. Reson. Med.: Off. J. Soc. Magn. Reson. Med./Soc. Magn. Reson. Med. 2014; 72:1599–1609. http://dx.doi.org/10.1002/mrm.25071.

[24]. Ohliger MA, Larson PE, Bok RA, Shin P, Hu S, Tropp J, et al. Combined parallel and partial Fourier MR reconstruction for accelerated 8-channel hyperpolarized carbon-13 in vivo magnetic resonance Spectroscopic imaging (MRSI). J. Magn. Reson. Imaging: JMRI. 2013; 38:701–713. http://dx.doi.org/10.1002/jmri.23989. [PubMed: 23293097]

[25]. Shin PJ, Larson PEZ, Uecker M, Reed GD, Kerr AB, Tropp J, et al. Chemical shift separation with controlled aliasing for hyperpolarized (13) C metabolic imaging. Magn. Reson. Med.: Off. J. Soc. Magn. Reson. Med./Soc. Magn. Reson. Med. 2014 http://dx.doi.org/10.1002/mrm.25473.

[26]. Gordon, JW.; Machingal, S.; Kurhanewicz, J.; Vigneron, DB.; Larson, PEZ. Ramp-sampled, symmetric EPI for rapid dynamic metabolic imaging of hyperpolarized C-13 substrates on a clinical MRI scanner. Proceedings of the Rd Annual Meeting of ISMRM; 2015;

[27]. Vasanawala, SS.; Murphy, MJ.; Alley, MT.; Lai, P.; Keutzer, K.; Pauly, JM., et al. Practical parallel imaging compressed sensing MRI: summary of two years of experience in accelerating body MRI of pediatric patients. 2011 8th IEEE International Symposium on Biomedical Imaging (ISBI 2011); 2011; p. 1039-1043.doi:http://dx.doi.org/10.1109/ISBI.2011.5872579

[28]. Lustig M, Donoho DL, Santos JM, Pauly JM. Compressed sensing MRI. IEEE Signal Proc. Mag. 2008; 25:72–82. http://dx.doi.org/10.1109/MSP.2007.914728.

[29]. Lustig M, Donoho D, Pauly JM. Sparse MRI: the application of compressed sensing for rapid MR imaging. Magn. Reson. Med.: Off. J. Soc. Magn. Reson. Med./Soc. Magn. Reson. Med. 2007; 58:1182–1195. http://dx.doi.org/10.1002/mrm.21391.

[30]. Heinig G, Jankowski P. Kernel structure of block Hankel and Toeplitz matrices and partial-realization. Linear Algebra Appl. 1992; 175:1–30.

[31]. Cadzow JA. Signal enhancement – a composite property mapping algorithm. IEEE Trans. Acoust. Speech. 1988; 36:49–62. http://dx.doi.org/10.1109/29.1488.

[32]. Subspace-Based Signal Analysis Using Singular Value Decomposition. 2009. p. 1-32.

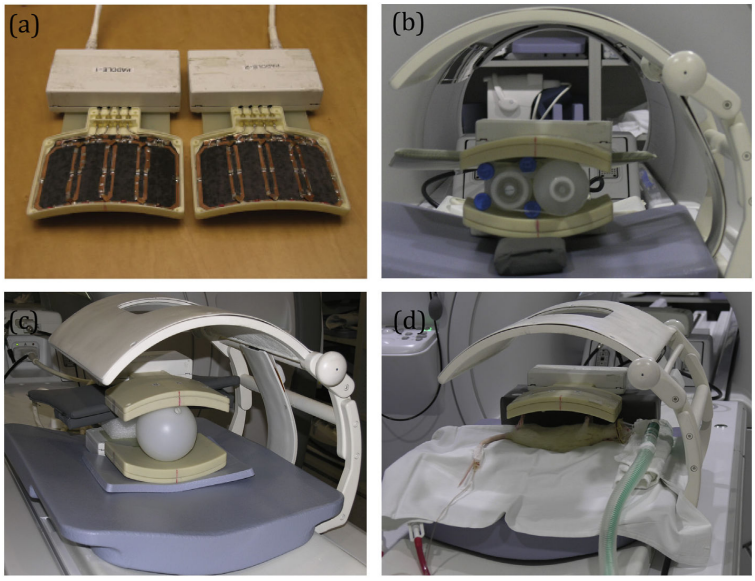

Fig. 1.

(a) Eight-channel ^{13}C receive coil with a linear arrangement of four coil elements in each housing. (b) Ethylene glycol phantom study set-up. (c) HP ^{13}C-pyruvate phantom set-up. (d) *In vivo* rat study set-up.

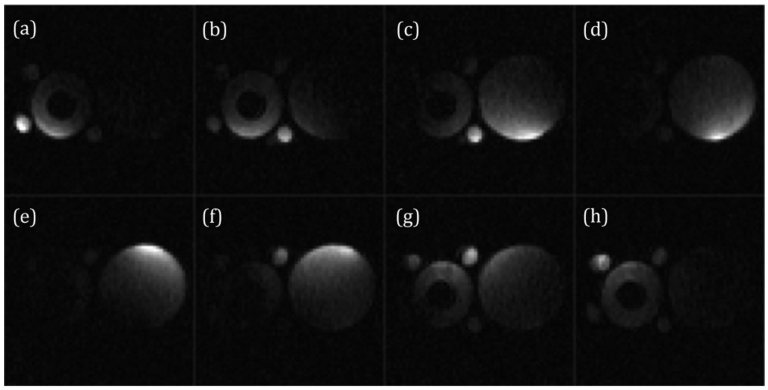

Fig. 2.

Individual coil images (a–h) of the fully sampled ethylene glycol phantom. Two paddle-shaped coil compartments are set up as shown in Fig. 1(b).

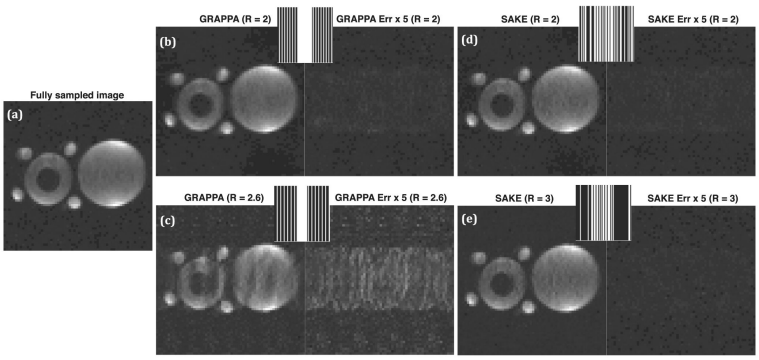

Fig. 3.

Comparison between fully sampled and under sampled ethylene glycol phantom images. (a–e) are individually scaled against their maximum signal intensities. (a) fully-sampled image (b and c) each panel has the reconstructed image (left), 5 times the error between the reconstruction and the fully sampled image (right) and the undersampling patterns (center top). (b) GRAPPA reconstruction with 2-fold under sampled data. The central ACS has 16 lines and the outer k-space is 3-fold under sampled. The mean square error (MSE) compared to (a) is 2.70×10^{-4}. (c) GRAPPA reconstruction with 2.6-fold under sampled data. ACS has 12 lines and the outer k-space is 4-fold under sampled. MSE is 2.70×10^{-3}. (d) SAKE reconstruction based on a 2-fold under sampled data. MSE is 2.67×10^{-4}. (e) SAKE reconstruction based on a 3-fold under sampled data, MSE is 4.38×10^{-4}.

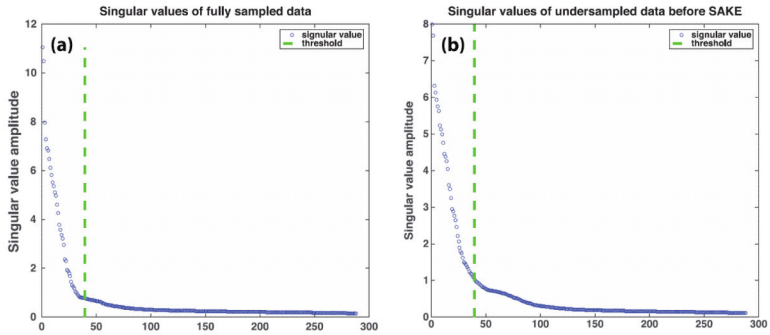

Fig. 4.

Singular values of the block Hankel data matrix A from the (a) fully sampled and (b) zero-filled under-sampled k-space data. The green dashed line indicates the threshold that divides the signal space from the discarded noise space. This threshold is determined in (a) as the point of maximum curvature. The corresponding rank of the A matrix (normalized by window size (6 × 6)) is 1.1 for the fully sampled phantom data (Fig. 3(a)). (For interpretation of the references to color in this figure legend, the reader is referred to the web version of this article.)

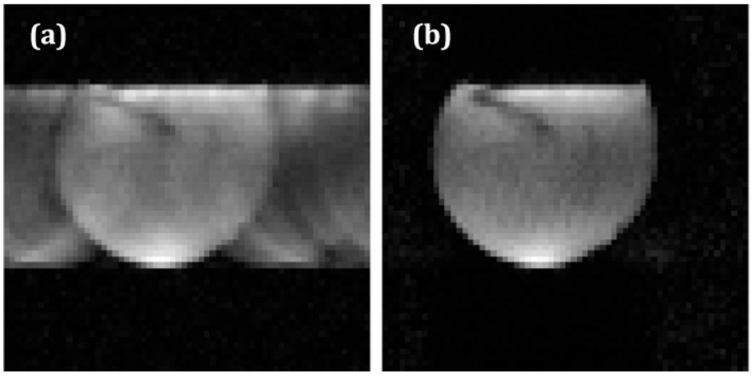

Fig. 5.

HP ^{13}C-pyruvate phantom images (a) zero-filled after 2-fold under sampling on the phase encode direction (b) SAKE reconstruction.

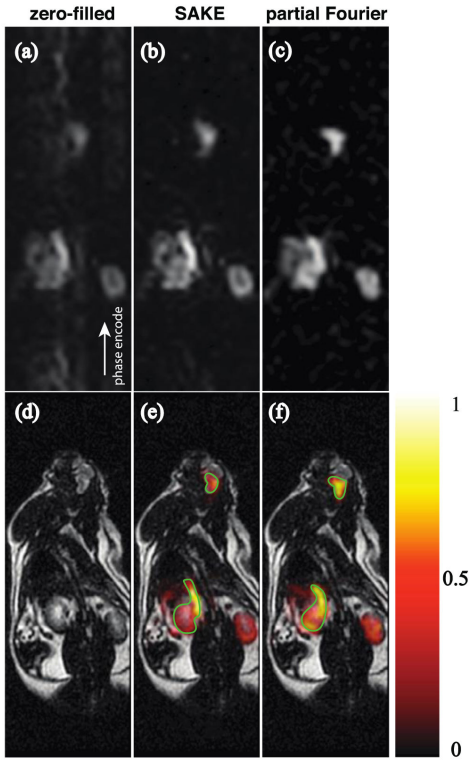

Fig. 6.

In vivo rat experiment with HP ^{13}C-t-butanol, (a), (b) and (c) are ^{13}C images of a coronal slice of 2 mm thickness. (a) Zero-filled image after 2-fold under-sampling on the phase encode (top to bottom) direction (b) SAKE reconstructed image based on the under-sampled image in (a). (c) Partial Fourier reconstruction with 25% over sampling. (d) ^{1}H T_2 FSE reference image of the 15 mm coronal slice. (e) SAKE reconstruction overlaid on the ^{1}H FSE image, two ROIs are drawn to cover one kidney and the brain. The ^{13}C signal intensity ratio between the kidney and the brain is 0.93. (f) Partial Fourier reconstruction overlaid on ^{1}H FSE, similar ROIs are drawn and ^{13}C signal intensity ratio between the kidney and brain is 1.08.